Mechanical Systems and Signal Processing 246 (2026) 113881

Contents lists available at ScienceDirect

Mechanical Systems and Signal Processing

journal homepage: www.elsevier.com/locate/ymssp

Full Length Article

Damage localization in bridges using curvature profiles identified from acceleration data via continuous wavelet transform

Sheng-Wang Zhang [a,b,*], Said Quqa [b,**], Antonio Palermo [b], Alessandro Marzani [b], Zhao-Hui Lu [a]

[a] State Key Laboratory of Bridge Safety and Resilience, Beijing University of Technology, No. 100 Pingleyuan, 100124 Beijing, China
[b] Department of Civil, Chemical, Environmental, and Materials Engineering, University of Bologna, Viale del Risorgimento 2, 40136 Bologna, Italy

ARTICLE INFO

Keywords:
Damage localization
Curvature profile
Continuous wavelet transform
Vehicle-bridge interaction
Structural health monitoring

ABSTRACT

Damage identification methods based on traffic-induced vibration data have gained significant attention in structural health monitoring of bridges, driven by the need for cost-effective sensing solutions. Recent studies have demonstrated that bridge curvature profiles can be identified from sparse acceleration measurements collected during vehicle passages using standard accelerometers. However, existing approaches for estimating curvature from acceleration data often struggle to suppress dynamic effects induced by moving vehicles. These methods typically rely on low-pass filters with a rigid cutoff threshold, which can compromise accuracy, especially during high-speed vehicle passages. To overcome this limitation, this study introduces a novel approach based on the continuous wavelet transform to isolate the quasi-static curvature profile and effectively remove dynamic components. The method is tested on a model that incorporates vehicle-bridge interaction effects and road roughness. Sensitivity analyses show that the proposed method outperforms standard filtering techniques across various sensor configurations, damage locations, severities, and multiple damage scenarios, even at relatively high vehicle speeds. Validation using field data further confirms the effectiveness and generality of the proposed approach.

1. Introduction

Bridges are essential components of modern transportation infrastructure. Over time, cyclic loading and environmental factors can accelerate material degradation and lead to structural damage, compromising their safety. Timely and accurate assessment of bridge health is therefore crucial for planning effective maintenance and intervention strategies.

In the last decades, vibration-based structural health monitoring (SHM) has gained significant attention for detecting anomalies in bridges [1–3]. Various algorithms have also been developed to localize damage using vibration data [4–6]. However, these methods often rely on dense sensor networks, leading to high instrumentation costs. To overcome this issue, the mechanical and dynamic effects induced by moving loads have been recently exploited to achieve effective anomaly detection and damage localization while limiting the instrumentation costs [7]. In particular, influence lines have emerged as a robust tool for deriving damage-sensitive indicators with clear physical interpretation [8–10].

* Corresponding author at: State Key Laboratory of Bridge Safety and Resilience, Beijing University of Technology, No. 100 Pingleyuan, 100124 Beijing, China.
** Corresponding author.
E-mail addresses: shengwang.zhang@unibo.it (S.-W. Zhang), said.quqa2@unibo.it (S. Quqa).

https://doi.org/10.1016/j.ymssp.2026.113881
Received 30 May 2025; Received in revised form 12 December 2025; Accepted 8 January 2026
Available online 16 January 2026

Influence lines derived from displacement [11–14] or strain [15–17] measures are mature techniques thoroughly discussed in the literature. However, displacement transducers can be expensive and need for a fixed reference point, which is typically challenging to find in long-term field applications [18]. Strain measurements, on the other hand, were proved to be reliable only close to the sensor positions [19,20].

Recently, Quqa et al. [21–23] proposed a method to identify curvature profiles, which can be interpreted as proportional to curvature influence lines for simply supported structures, directly from acceleration responses. This method is particularly attractive for damage localization, as acceleration signals can be efficiently collected using cost-effective sensor networks with standard accelerometers. Within this framework, the approach proposed by Quqa et al. enables the derivation of a spatially dense damage index from curvature profiles reconstructed with sparse accelerometer networks, such as those commonly used in vibration-based SHM. The method relies on filtering the acceleration response to isolate its quasi-static component, associated with the structural deflection induced by a moving vehicle, which can then be interpreted as a curvature profile by exploiting fundamental static relationships. Lu et al. [24] further investigated this method using laboratory experiments to verify its effectiveness and accuracy. While effective, this method can suffer from reduced localization accuracy at high vehicle speeds. This limitation stems from the use of a low-pass filter with a rigid cutoff, which may inadequately separate dynamic components from the quasi-static response.

The main challenge in applying low-pass filtering for high-speed applications is that the quasi-static component of the structural acceleration response (representative of the curvature profile) can partially overlap with dynamic components of the bridge vibration caused by resonant modes. In such cases, a rigid frequency cutoff used in traditional low-pass filters removes all content above the threshold, potentially discarding higher-frequency elements that are essential for capturing sharp features of the response, such as the peak of a triangular quasi-static response. This limitation highlights the need for a more flexible thresholding approach that can better preserve the shape of the extracted component.

In this context, the continuous wavelet transform (CWT) [25] emerges as a promising tool. CWT has been extensively investigated for signal processing for SHM [13,26–31]. However, previous applications of CWT to acceleration signals have primarily focused on analyzing variations in the energy distribution of dynamic components, rather than exploiting the wavelet transform to extract or examine quasi-static components [30,31].

The key idea of this paper is instead to apply the CWT to the bridge acceleration response induced by a moving vehicle to extract its quasi-static response. This is achieved by exploiting a set of scaled versions of a mother wavelet whose shape resembles the expected quasi-static response (e.g., nearly triangular). These components are then isolated and used to efficiently approximate the ideal quasi-static response.

The method is particularly appealing due to the compactness of the wavelet in time and the flexibility to choose its shape based on specific requirements [32]. Unlike Fourier bases, which have a strictly defined frequency content [33], an appropriate selection of the mother wavelet enables the decomposition of a signal into components with distinct waveforms, even when their frequency representations overlap.

The proposed method is demonstrated using simulated datasets that incorporate vehicle-bridge interaction (VBI) effects and road roughness, highlighting its advantages over existing state-of-the-art approaches. Robustness is assessed through sensitivity analyses involving various sensor configurations, damage scenarios, and vehicle speeds. Additionally, a real-world case study is analyzed to validate the effectiveness and generality of the method in real and more complex applications.

2. Theoretical background

2.1. Curvature profile from acceleration data

The acceleration response of a bridge induced by a traveling load can be modeled as the superposition of a dynamic component (due to the inertial effects) and a quasi-static component (resulting from the static deflection of the beam under the moving load).

Consider a single load P moving at constant speed v on a simply supported Euler-Bernoulli beam having flexural rigidity EI and

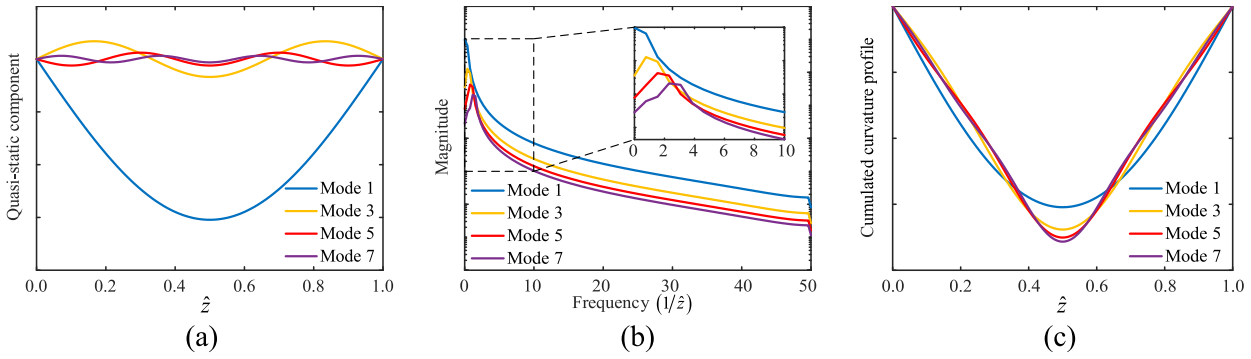

Fig. 1. Quasi-static components of the structural response calculated at $\zeta = 1/2$: (a) in the space domain, (b) in the frequency domain, and (c) cumulated curvature profile.

length L, being E the Young's Modulus and I the cross-section moment of inertia. A closed-form solution of the acceleration (denoted as $\ddot{y}_B(z,t)$, where t denotes the time variable) at a fixed reference section z (i.e., a sensor location on the bridge) can be represented as [34]:

$$\ddot{y}_B(z,t) = \frac{2PL^3}{\pi^4 EI}\sum_{m=1}^{\infty}\sin\left(\frac{m\pi z}{L}\right)[\lambda_m(t) + p_m(t)] \tag{1}$$

where $\lambda_m(t)$ and $p_m(t)$ are the quasi-static and dynamic components of the acceleration response, respectively, projected on the m-th mode shape of the structure.

In this formulation, the dynamic component is separated into individual modal responses, while the quasi-static component (defined as the acceleration of a point moving under the applied load while neglecting inertial effects and considering only elastic deformation) is decomposed into its sine components (shown in Fig. 1(a)), as follows:

$$\lambda_m(t) = -\left(\frac{\pi v}{mL}\right)^2 \sin\left(\frac{m\pi v t}{L}\right) \tag{2}$$

The time dependence in Eq. (2) is only determined by the changing load location, i.e., the space traveled by the moving load ($\widehat{z} = vt$). Previous studies [22,23] have shown that, under constant vehicle speed, the quasi-static component of the acceleration structural response is proportional to the curvature profile of the structure generated by a point load applied at location z. This relationship is grounded in the Maxwell-Betti reciprocal work theorem, according to which, the displacement profile induced by a point load at a fixed location (say z) is equivalent to the displacement influence line at that same location, that is, the displacement in z as a function of position of the moving load ($\widehat{z}$). When the sensor measures acceleration, it captures the time second-order derivative of displacement. In the quasi-static regime and under constant speed (v), this time second-order derivative can be related to the position of the moving load ($\widehat{z} = vt$). By applying the reciprocity principle, the second-order derivative with respect to time becomes equivalent to the second spatial derivative of the displacement profile induced by a point load moving along the structure, i.e., the curvature profile.

In this condition, the quasi-static component can be interpreted as a representation of the bridge curvature in section z as a function of $\widehat{z}$. Introducing the nondimensional variable $\zeta = z/L$ that represents the sensor position normalized to the beam length, the curvature profile (denoted as $h^{(\zeta)}[\widehat{z}]$) can be expressed as:

$$h^{(\zeta)}[\widehat{z}] = -\frac{2PLv^2}{\pi^2 EI}\sum_{m=1}^{\infty}\frac{1}{m^2}\sin(m\pi\zeta)\sin\left(\frac{m\pi\widehat{z}}{L}\right) \tag{3}$$

Fig. 1 shows the contributions of the components of Eq. (3) calculated for different modes (a), as well as their frequency representations (b), and the cumulated results (c), which tends to a triangular shape, corresponding to the curvature profile induced by a point load. This highlights the importance of higher-frequency components in accurately reconstructing the curvature profile. It is important to note that the frequencies shown here do not correspond to the natural frequencies of the structure, but rather to spatial frequencies (represented in Fig. 1(b)), i.e., the inverse of the mode shape wavelength. Since the vehicle moves at constant speed, these spatial frequencies can be mapped onto the time domain and interpreted as effective temporal frequencies. These effective frequencies are generally lower than the natural frequencies of the structure and vary with the vehicle speed.

However, when the components with relatively higher frequency approach or overlap with the dynamic components (particularly for high-speed vehicles, where the effective frequencies become comparable to the natural frequencies of the structure), the conventional filtering method used for separating quasi-static and dynamic components becomes less effective. In this case, a large cutoff threshold allows residual dynamic components to distort the curvature profile, while a small threshold suppresses the high-frequency part of the quasi-static response, resulting in an overly smooth curvature estimate.

Although this interpretation applies in general to statically determinate Euler-Bernoulli beams, where the curvature profile is piecewise linear, the theoretical background of this paper focuses on simply supported beam-like structures, for ease of interpretation. Nevertheless, the approach can be applied to a wider range of structures, in which the local variation of the quasi-static component is sensitive to local damage while the rigorous interpretation in terms of curvature does not hold, as shown in Section 6.

2.2. Continuous wavelet transform

As anticipated, the core idea is to exploit the CWT to estimate the curvature profile from acceleration responses. The CWT of a signal $x(t)$ can be defined as [32]:

$$W_{x,\psi}(b,s) = \frac{1}{\sqrt{|s|}}\int_{-\infty}^{\infty} x(t)\psi^*\left(\frac{t-b}{s}\right)dt \tag{4}$$

where $W_{x,\psi}(b,s)$ represented as the wavelet coefficient; $\psi^*(t)$ is the complex conjugate of $\psi(t)$, which is the basis function of the wavelet transform, also referred to as the "mother wavelet"; b is a translation factor in time; and s is the scaling factor, which is inversely proportional to the center frequency of the scaled wavelet function.

At the same time, when $W_{x,\psi}(b,s)$, $\psi(t)$, b and s are known, the time domain signal $x(t)$ can be reconstructed based on the inverse continuous wavelet transform (iCWT) process, which is defined as [35]:

$$x(t) = \int_{-\infty}^{\infty} \int_{-\infty}^{\infty} W_{x,\psi}(b,s)\psi\left(\frac{t-b}{s}\right) dsdb \tag{5}$$

As shown by Eqs. (4) and (5), the CWT provides the time-scale (or time-frequency) representation of the input signal, while the iCWT reconstructs it in the time domain. By adjusting the integration limits in Eq. (5), one can isolate specific scale (or frequency) ranges and time intervals of interest, thereby enabling both filtering and time windowing. This capability will be exploited to extract the quasi-static component of the acceleration response that will be used for damage localization, as further detailed in Section 3.2.

Curvature profiles for simply supported beams under a point load have a triangular shape. This study uses the generalized Morse wavelet (GMWs) [36] as a mother wavelet with a shape that resembles a triangle [36–39], which can be represented as:

$$\psi_{P,\gamma}(\omega) = U(\omega) a_{P,\gamma} \omega^{\frac{P^2}{\gamma}} e^{-\omega^{\gamma}} \tag{6}$$

where $U(\omega)$ is the unit step function, $a_{P,\gamma}$ is a normalizing constant, P^2 is the time-bandwidth product, and the parameter γ characterizes the symmetry of the GMW [37]. In this study, γ is chosen to be 3 to make the wavelet symmetric, while P^2 is set to 3 to make the wavelet cover the smallest frequency range [36].

Fig. 2 shows time and frequency domain representations of the natural GMW (i.e., considering the unscaled function, $s = 1$). The representations highlight the compact support in both time and frequency. Specifically, the compactness in time makes it suitable to describe local phenomena in the signal (such as local stiffness variations, for instance, due to damage [22]) while its compactness in frequency makes it suitable for separating signal components with different frequency contents and isolating local distortions potentially due to damage.

Moreover, as shown in Fig. 2(b), the $s = 1$ wavelet function corresponds to a specific center frequency f_c:

$$f_c = \frac{1}{2\pi}\left(\frac{P^2}{\gamma^2}\right)^{1/\gamma} \tag{7}$$

which in this case is equal to 0.11 Hz but spans a wide frequency range. This characteristic distinguishes it from the Fourier basis, which is confined to a narrow frequency band.

3. Proposed damage localization method

After collecting the acceleration time histories at selected instrumented locations during vehicle passages in both the "baseline" and "possibly damaged" conditions (Fig. 3(a)), the proposed identification procedure can be applied. The process, also illustrated in Fig. 3, consists of the following steps:

1) Signal pre-processing: a time range of interest of the signal is selected and a padding process is applied to mitigate boundary effects (Fig. 3(b));
2) Curvature profile identification: the CWT is applied to transform the time-domain signal into a time-scale representation, i.e., the scalogram (Fig. 3(c)). Then, a portion of the time-scale diagram is selected corresponding to large wavelet scales (i.e., low frequencies) as well as the original time range before padding (Fig. 3(d)). In these intervals, the iCWT is applied using only the selected low-frequency components to reconstruct the quasi-static signal, which can be interpreted as a curvature profile - or, for structures differing from an Euler-Bernoulli beam, as a curvature-like feature (Fig. 3(e));

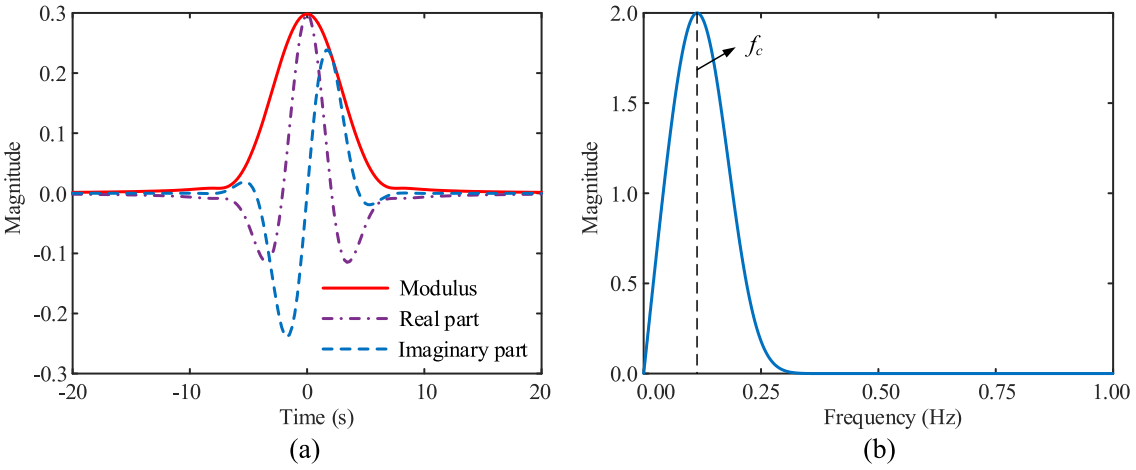

Fig. 2. Unscaled Morse wavelet: (a) time-domain representation, (b) frequency-domain representation.

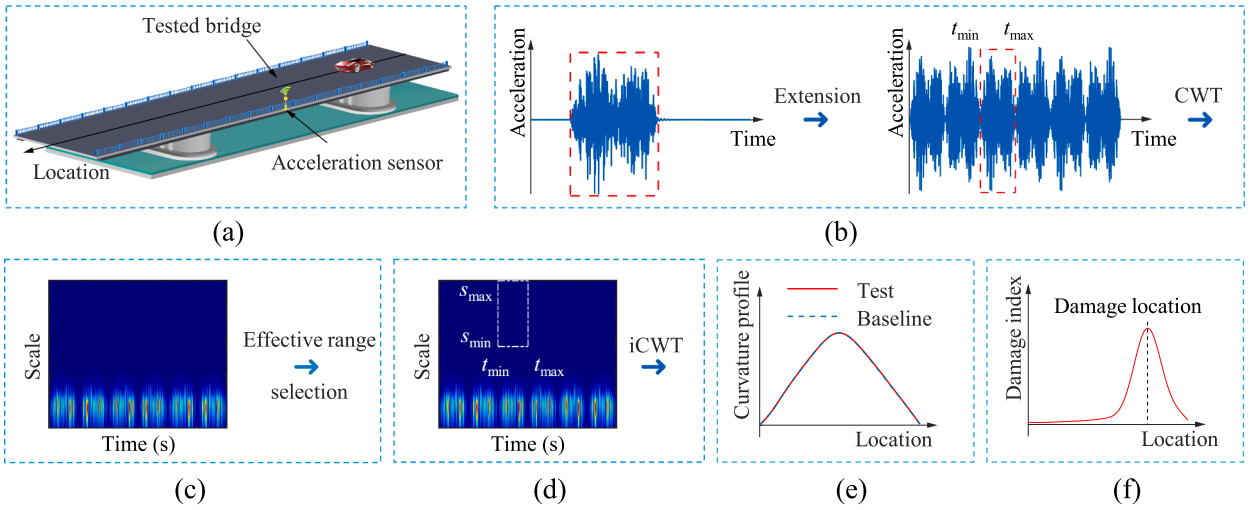

Fig. 3. Scheme of the proposed identification procedure: (a) acquisition of the bridge response, (b) signal pre-processing, (c) calculation of the CWT scalogram, (d) effective range selection, (e) curvature profile identification, (f) damage index calculation.

3) Damage index calculation: the estimated curvature profiles are compared to a baseline configuration at periodic intervals to identify any differences that potentially indicate structural damage (Fig. 3(f)).

3.1. *Signal pre-processing*

When the CWT is evaluated near the signal boundaries, it performs a convolution between the scaled wavelet function (which can be seen as a filter impulse response) and the initial or final portion of the acceleration signal. At very low or high time-shift indices (i.e., close to the start or end of the signal) this convolution cannot be computed correctly, as the filter impulse response would extend beyond the available data. In signal processing, replication or mirroring of the signal is a standard approach to address this limitation [40].

For the proposed method, a pre-processing step is applied to the acceleration signal with this purpose. First, the signal is trimmed to the time interval between the vehicle entering and leaving the bridge (i.e., $t_{\min}$ and $t_{\max}$, respectively), which can be accurately identified using laser barriers positioned at the edges of the bridge. Then, to avoid the aforementioned issues at boundaries, the selected signal is extended by mirroring it with reversed sample order and inverted sign multiple times, as illustrated in Fig. 3(b). This creates a longer signal where only the outermost segments are affected by the boundary limitations. This approach also ensures that the low-frequency components of the signal approach zero when the vehicle is near the structural boundaries, which aligns with the physical expectation that the quasi-static curvature of a simply supported bridge vanishes at the ends.

3.2. *Curvature profile identification*

As discussed in Section 2.1, for Euler-Bernoulli beams, the quasi-static component of the acceleration response can be interpreted as the curvature profile of a beam subjected to a point load. To retrieve this information, the proposed CWT-based method is used to isolate the quasi-static component from the full acceleration signal measured by the accelerometers.

First, the CWT is applied to transform the time-domain acceleration signal into a time-scale representation. To facilitate the CWT process, a CWT filter bank at specified scale values is first established. Specifically, this filter is formed of a set of scaled versions of the mother wavelet function that, convoluted with the input signal, result in the wavelet coefficients at different scales (as illustrated in Eq. (4)). The energy of these components can be depicted on a time-scale map and represents the scalogram reported in Fig. 3(c).

The scales included in the filter bank are determined by the lowest and highest usable pseudo-frequencies. The minimum admissible frequency depends on the signal length, since wavelets with excessively large temporal support cannot be meaningfully applied. The maximum admissible frequency is constrained by the Nyquist limit, $f_{\mathrm{h}} = F_s/2$ (where F_s denotes the sampling frequency), which prevents aliasing. To obtain finer resolution at low frequencies, the usable frequency interval is discretized on a logarithmic grid. Specifically, the frequency range is divided into octaves, and each octave is split into ten logarithmic substeps, resulting in the frequency sequence:

$$f_k = 2^{-k/10} f_{\mathrm{h}}, k = 1, \cdots, n-1 \tag{8}$$

where n is the total number of wavelets in the filter bank. Each pseudo-frequency is then mapped to its corresponding scale through the standard CWT scaling law:

$$s_k = \frac{f_c F_s}{f_k} \tag{9}$$

Next, a portion of the total time-scale representation is selected to isolate the quasi-static component of interest. The bounds of this interval, denoted $s_{\min}$ and $s_{\max}$, are chosen as follows. Because the quasi-static component exhibits a triangular shape in the time domain, and the generalized Morse wavelet closely resembles this shape, the quasi-static content is concentrated at large scales. Accordingly, $s_{\max}$ is set equal to the largest scale allowed by the signal length. Conversely, $s_{\min}$ is chosen such that its associated pseudo-frequency remains below the first natural frequency of the bridge, thereby excluding dynamic contributions (see Section 4.4 for a sensitivity analysis).

Finally, the curvature profile is reconstructed by performing the iCWT using only the selected wavelet components, as follows:

$$x_{\text{filtered}}(t) = \int_{t_{\min}}^{t_{\max}} \int_{s_{\min}}^{s_{\max}} W_{x,\psi}(b,s)\psi\left(\frac{t-b}{s}\right) ds db \tag{10}$$

where $t_{\min}$ and $t_{\max}$ are the time indices that represent the original (unpadded) portion of the signal.

It is worth noting that, although selecting $s_{\min}$ may appear analogous to applying a hard frequency cutoff, each wavelet at a given scale spans a broad frequency band. This overlap naturally includes higher-frequency content that is essential for accurately reproducing waveform features such as sharp peaks. Consequently, the reconstructed signal retains greater fidelity and exhibits less smoothing than signals obtained using traditional low-pass filters with rigid cutoff thresholds. Moreover, performing filtering in the Fourier domain implicitly decomposes the signal into a basis of harmonic functions with infinite temporal support [41]. Accurately representing localized distortions in this framework requires a large number of Fourier components. In contrast, the compactness of wavelet functions in time and frequency makes them inherently well suited for capturing short-duration, localized phenomena.

3.3. Damage index

In practice, structural damage is typically assessed by comparing a "baseline" condition of the structure with a "test", i.e., possibly damaged, condition [23]. In this study, damage is modeled as a localized loss of flexural stiffness. Since the structure is assumed statically determinate in this study, changes in the curvature profile due to damage are confined to the vicinity of the damaged region. Consequently, the damage index (defined as the difference between curvature profiles identified under the baseline and test conditions) will exhibit a peak at the damage location.

In real-world conditions, collected signals are affected by factors such as instrumentation noise, road roughness, and VBI effects. These influences can reduce the accuracy of curvature profiles derived from individual vehicle passages. To mitigate this limitation, averaging the curvature profiles over multiple passages can enhance the robustness and reliability of the resulting damage index [7]. Thus, a damage index $D[\widehat{z}]$ can be defined as follows:

$$D[\widehat{z}] = \frac{\sum_{i=1}^{r_{\text{test}}} h_{d_i}^{(\zeta)}[\widehat{z}]}{r_{\text{test}}} - \frac{\sum_{i=1}^{r_{\text{baseline}}} h_{b_i}^{(\zeta)}[\widehat{z}]}{r_{\text{baseline}}} \tag{11}$$

where $h_{d_i}^{(\zeta)}[\widehat{z}]$ and $h_{b_i}^{(\zeta)}[\widehat{z}]$ are curvature profiles identified at a sensor section ζ with i-th vehicle passage for the test and baseline conditions, respectively, and r_{test} and r_{baseline} are the number of vehicles considered for the test and baseline conditions, respectively.

While the proposed method assumes that the vehicle travels at nearly constant speed during each passage, different passages may naturally occur at different speeds. This variation affects the quasi-static component only by changing its duration in time and, consequently, the number of spatial samples obtained given the sampling frequency of the acquisition system. When different passages yield curvature profiles with different numbers of samples, they can be mapped onto a common spatial grid using simple linear interpolation before calculating the average, as demonstrated in [22,23].

4. Numerical benchmark

A numerical benchmark based on a VBI model is used to simulate the responses of simply supported bridge decks in both

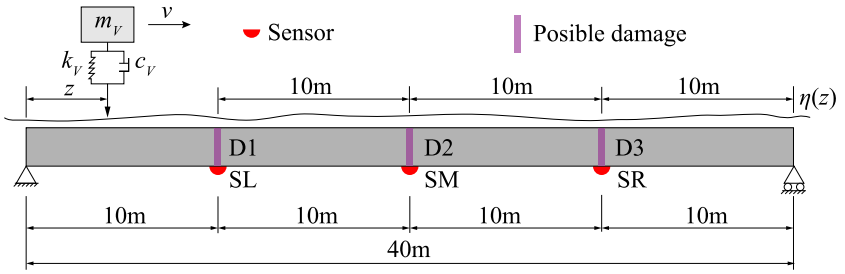

Fig. 4. Scheme of the VBI system.

undamaged and damaged conditions. Road roughness is also included to account for surface irregularities. This setup is employed to evaluate the damage localization performance of the proposed method.

4.1. Vehicle-bridge interaction model

The structure considered here is schematized as a 40 m long simply supported beam with an elastic modulus $E = 3 \times 10^{10}$ N/m^2 and a cross-sectional moment of inertia $I = 3.532$ m^4 [23] (see the scheme in Fig. 4). The mass per unit length m_B is 10000 kg/m. The beam is modeled using one-dimensional elements with a spatial discretization of 0.25 m. The first four modal frequencies of the bridge are 3.196 Hz, 12.783 Hz, 28.7612 Hz, and 51.132 Hz, respectively. Rayleigh damping is adopted to simulate structural dissipation. The Rayleigh coefficients are computed from the first two resonant modes, for which a damping ratio of 5% is prescribed.

The vehicle is modeled as a spring mass m_V of 1750 kg with a suspension spring stiffness k_V of 1.8×10^7 N/m and damping $c_V = 1.44 \times 10^5$ N·s/m [23,42]. With these parameters, the modal frequency of the vehicle is calculated as 16.141 Hz. The structural response is sampled at a rate of $F_s = 200$ Hz. These parameters are based on a real structure analyzed in a previous study [23]. The VBI model also includes road roughness, modeled as Class C in accordance with the ISO 8608 standard [43] based on the Power Spectral Density method [44].

The VBI system of equations (see Appendix A for details) is solved using the Newmark-beta method to obtain the dynamic responses of the bridge. Fig. 5 shows the displacement and acceleration collected at the mid-span (i.e., though sensor SM in Fig. 4) when a vehicle crosses the undamaged bridge with a speed of 5 m/s.

4.2. Estimation of the curvature profile from an individual vehicle run

The first test in this section aims to estimate the curvature profile from a single structural response, specifically the acceleration time history shown in Fig. 5(b). To reduce boundary effects introduced by the CWT, the signal pre-processing strategy described in Section 3.1 is applied before analysis. First, the effective range is defined as the interval during which the vehicle is on the bridge, i.e., $t_{\min} = 3.6$ s and $t_{\max} = 11.6$ s, as observed in Fig. 5. Then, the signal within the effective range is extracted and mirrored by reversing both its sign and sample order. The original and mirrored signals are then concatenated and repeated three times to generate an extended signal for wavelet analysis, as illustrated in Fig. 6.

Next, the CWT is applied to the pre-processed signal using a wavelet bank consisting of 132 scaled versions of the mother wavelet. This number results from the process described in Section 3.2. Fig. 7 shows the scalogram obtained by performing CWT for the pre-processed acceleration response.

The effective range highlighted by the white box in Fig. 7 is used to reconstruct the curvature profile. The selected scale limits are $s_{\min} = 53.8$ and $s_{\max} = 3224.4$. According to the inverse proportional relationship between scale and frequency (see Eq. (9)), these correspond to center frequencies $f_{\max} = 0.40$ Hz and $f_{\min} = 0.007$ Hz, respectively (see Section 4.4 for more details). The inverse CWT is then performed using only the selected components, while maintaining the same parameters as in the forward transform.

The resulting curvature profile estimated at the mid-span is shown in Fig. 8(a), with the corresponding time-scale representation provided in Fig. 8(b).

The extracted curvature profile exhibits a nearly triangular shape with its peak at the sensor location, closely matching the theoretical profile shown in Fig. 8(a). This indicates that the quasi-static component (i.e., the curvature profile) has been accurately extracted.

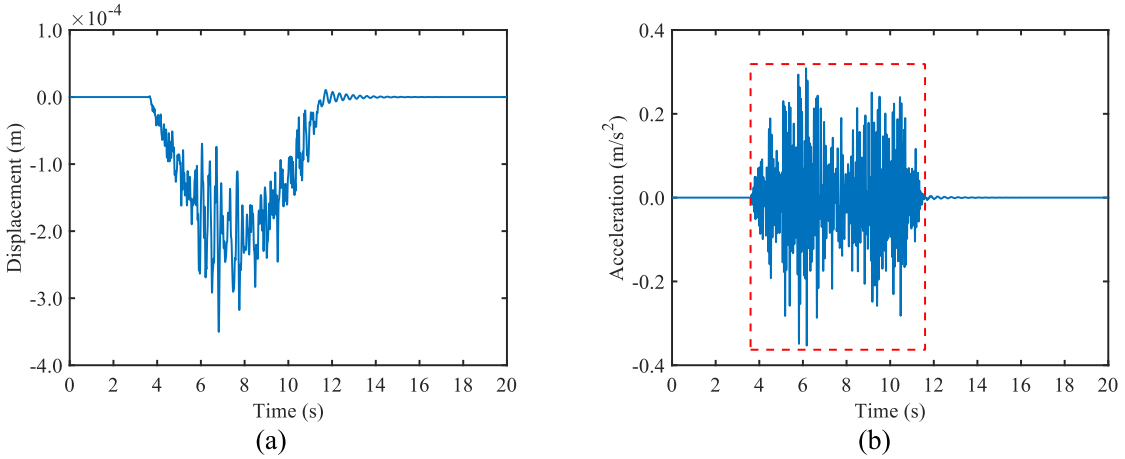

Fig. 5. Structural responses generated using the VBI model at the midspan: (a) displacement, (b) acceleration.

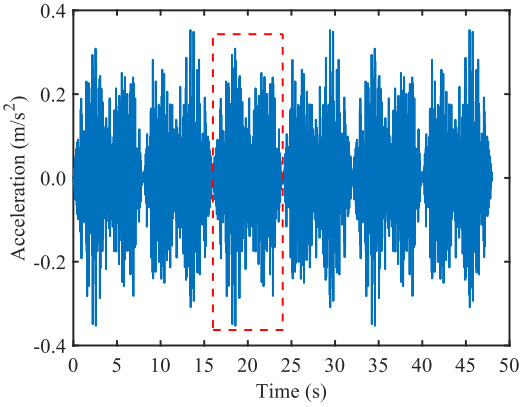

Fig. 6. Results of the signal pre-processing (the red box highlights the original portion of the signal).

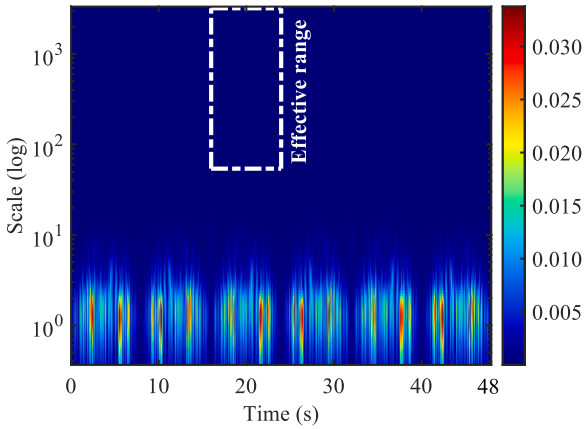

Fig. 7. Time-scale scalogram of the pre-processed acceleration signal.

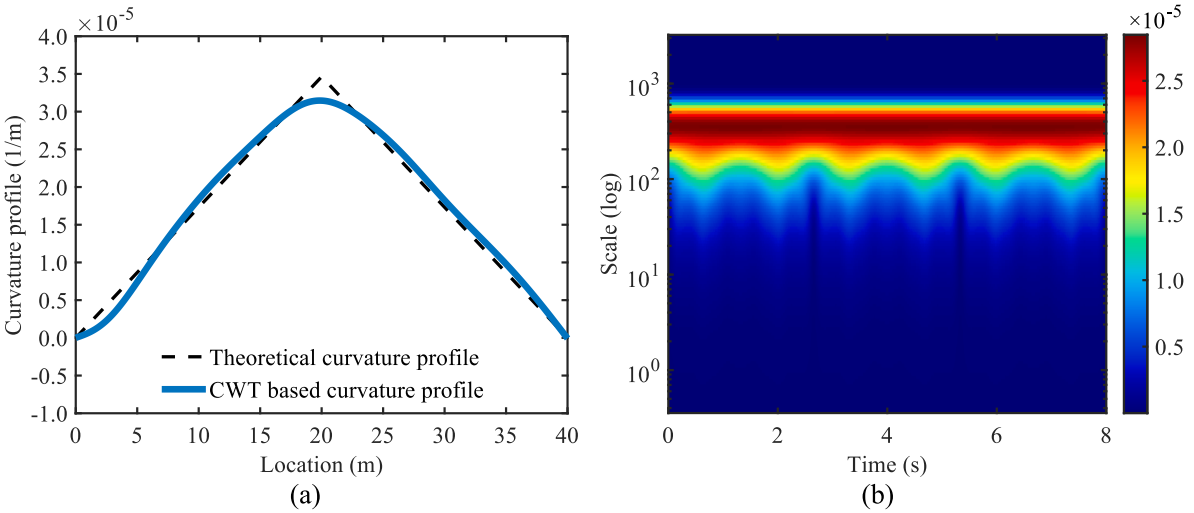

Fig. 8. Results of the extracted curvature profile: (a) curvature profile of the baseline condition of the bridge at the mid-span section, (b) time-scale scalogram of the baseline signal after the inverse CWT.

4.3. Damage localization from multiple vehicle runs

To evaluate the damage localization capability of the proposed approach, a damaged condition is simulated by reducing the elastic modulus of the element located at 30 m (i.e., D3 in Fig. 4) by 20%.

The procedure described in Section 4.2 is then repeated using the same vehicle and bridge parameters for two simulation sets: one with 100 vehicle passages over the baseline (undamaged) bridge and the other with 100 passages over the test (damaged) bridge. In both cases, road roughness profiles are changed randomly for each passage. Other vehicle parameters are kept constant in this test.

The curvature profiles obtained in the baseline and test conditions are then averaged, and a damage index is calculated according to Eq. (11). The mean curvature profiles for the two conditions are shown in Fig. 9 and resemble the reference profile presented in Fig. 8. The corresponding damage index is illustrated in Fig. 10.

Notably, the damage index exhibits a clear peak at 30 m along the bridge, corresponding to the location of the simulated damage at D3, while remaining low elsewhere. The robustness of this method under varying conditions will be further examined in the sensitivity analysis presented in Section 5.

4.4. Frequency threshold selection and comparison with state-of-the-art method

In the state-of-the-art approach based on low-pass filtering [21,23], the cutoff frequency defines a strict threshold: all frequency components above it are removed. This often produces an overly smoothed curvature profile, which may weaken the capability of identifying localized distortions due to damage. Increasing the cutoff frequency can partially mitigate this limitation by improving spatial localization, but it also reintroduces unwanted high-frequency content linked to the dynamic response, generating artefacts unrelated to damage.

Conversely, the CWT uses scaled versions of the mother wavelet, each spanning a broader frequency band (Fig. 2(b)). This wider coverage enables a more complete reconstruction of the triangular curvature profile, while still capturing short-duration irregularities associated with damage. This feature is particularly advantageous when vehicles travel at high speed.

In both approaches, selecting an appropriate threshold is critical for accurate curvature estimation and damage localization. In the lowpass filter-based method, this threshold is defined by the cutoff frequency, while in the proposed CWT-based method, it corresponds to the minimum scale $s_{\min}$ used in the reconstruction.

To compare the performance of both methods, damage localization is performed for the same bridge and road roughness profiles described in Section 4.3. The analysis is conducted using cutoff frequencies and corresponding $f_{\max}$ of 0.2 Hz, 0.3 Hz, 0.4 Hz, and 0.5 Hz for the lowpass filter-based and CWT-based methods, respectively. The comparison results, including the averaged curvature profiles and the damage indices, are shown in Figs. 11(a) and (b), for the proposed method and reference approach, respectively.

The identified curvature profiles (left panels) in Fig. 11 show that, for the same frequency threshold, vibration-induced fluctuations are more pronounced in the results of the state-of-the-art method, while the CWT-based method better preserves the expected triangular shape of the quasi-static curvature profile, with reduced interference from dynamic effects.

This distinction is further evident in the damage index plots (right panels). In all cases, increasing the frequency threshold sharpens the main peak of the damage index. However, in the reference method, the damage effect is reconstructed from a limited set of harmonics below the cutoff frequency, which can limit localization precision. In contrast, the CWT leverages scaled versions of the mother wavelet to more compactly and accurately represent the localized peak associated with damage.

As a result, the CWT-based method consistently identifies the damage location without ambiguity across all tested thresholds. Based on the outcomes shown in Fig. 11(a), the optimal frequency threshold for this 40 m simply supported beam is $f_{\max} = 0.40$ Hz, which provides a good balance between accurate damage localization and suppression of unwanted high-frequency components.

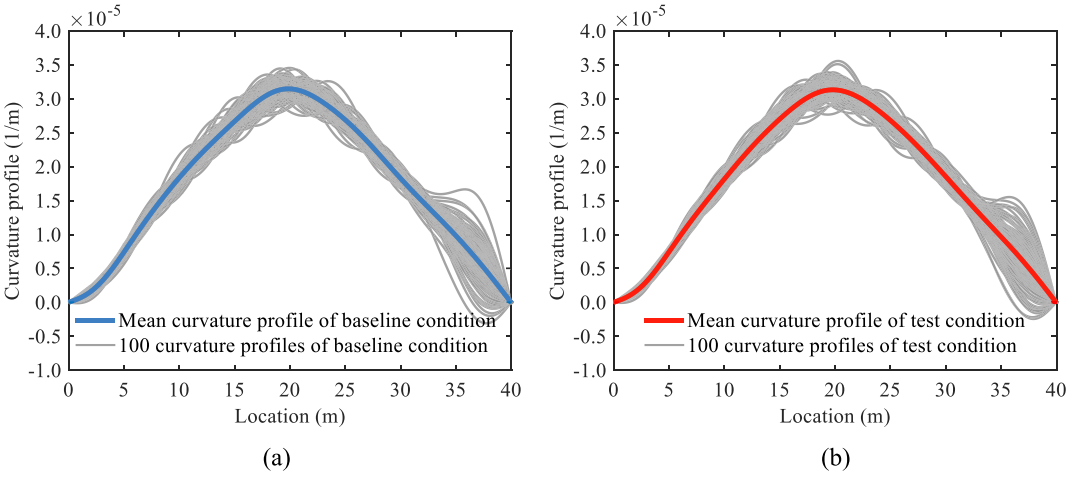

Fig. 9. Averaged curvature profiles: (a) baseline condition, (b) test D3 condition.

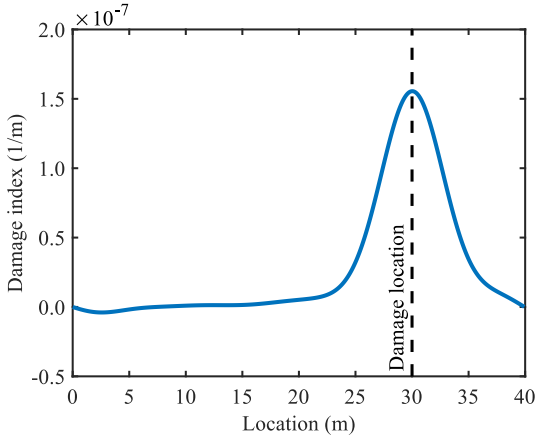

Fig. 10. Damage index for configuration D3.

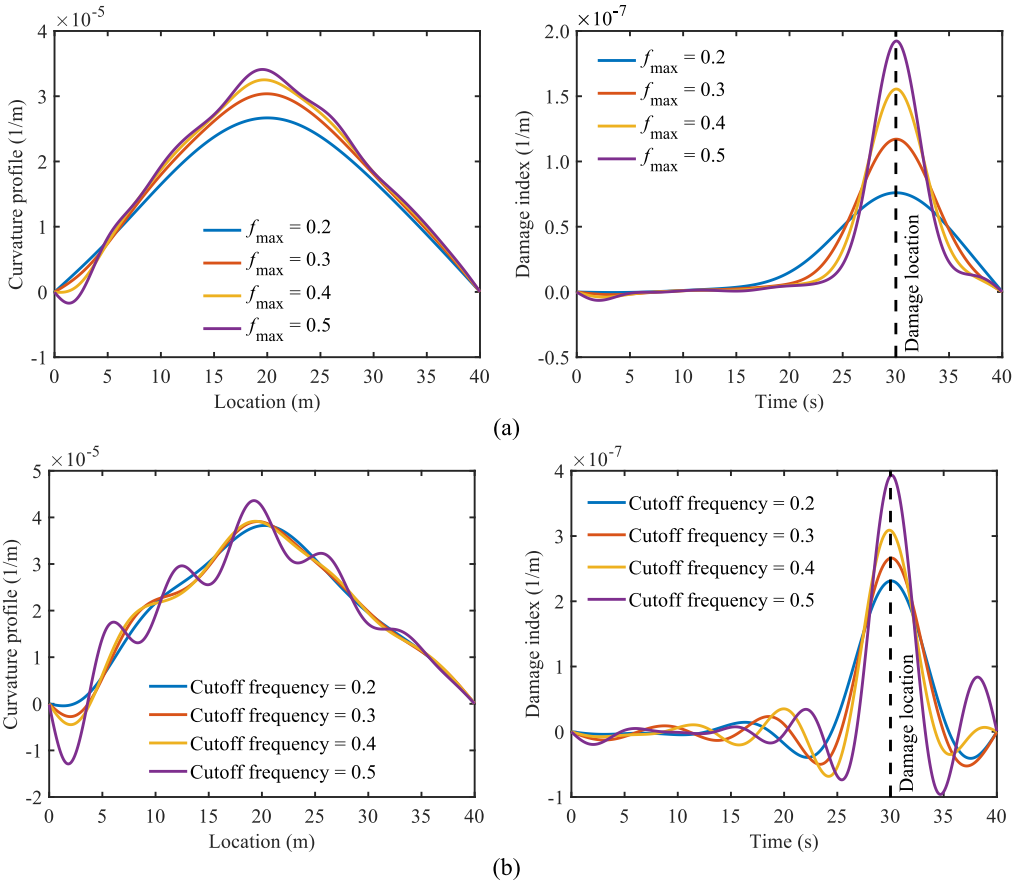

Fig. 11. Performance comparison with the conventional method: (a) proposed CWT-based method, (b) reference sate-of-the-art method.

However, variations in the selected threshold within the range discussed in Section 3.2 have only a minor impact on the overall performance of the method.

5. Sensitivity analysis

In this section, a sensitivity analysis is performed to test the robustness of the proposed method to (1) sensor parameters (position and noise level), (2) damage parameters (location, severity, spatial extension, and number), and (3) vehicle speed.

5.1. Sensitivity to sensor parameters

Two parameters are considered for the sensitivity analysis regarding the sensing instrumentation, namely the sensor position along the structure and the acquisition noise level, which are representative of different sensor models. First, the proposed procedure is applied using the structural response collected at three sensor positions (i.e., SL, SM, and SR in Fig. 4). A total of 100 tests were performed using the same parameters described in Section 4.3, assuming a vehicle speed of 5 m/s and a localized damage at position D3 with an extent of 0.25 m and a 20% reduction in stiffness. The averaged curvature profiles identified in the baseline configuration and the damage indices evaluated for the three sensor positions are presented in Fig. 12.

Notably, the shape of the averaged curvature profile changes in the three cases, showing a peak value at the sensor position. Nevertheless, the damage index has a sharp peak at the damage location, consistent across all sensor positions.

In field tests, a typical accelerometer for SHM applications is affected by noise with a signal-to-noise ratio (SNR) of 40–50 dB [45]. Different cases are then analyzed by adding white Gaussian noise components with SNR = 50 dB, 40 dB, and 30 dB to the recordings. Fig. 13 shows the damage index results for different SNRs obtained using sensor SM.

The comparison between Figs. 12(b) and 13 reveals a twofold impact of white Gaussian noise on the damage index. First, it can introduce spurious peaks at non-damaged locations. Second, it generally elevates the overall level of the damage index, reducing contrast. As the SNR increases, the peak associated with the actual damage becomes more pronounced, with higher kurtosis, making the damage location easier to identify. Conversely, high noise levels, as in the case of SNR = 30 dB, noticeably degrade the results. Despite this, under typical noise conditions (SNR between 40 dB and 50 dB), the proposed method remains effective in clearly identifying the damage location, even with a single sensor.

5.2. Sensitivity to damage parameters

To assess the robustness of the proposed method to different types of damage, multiple analyses are performed considering different damage locations, namely D1, D2, and D3 (see Fig. 4). In this case, a vehicle travels at a speed of 5 m/s on a bridge with a single damage characterized by a length of 0.25 m and a 20% reduction in element stiffness, with data collected from the SM sensor. The results for D3 (with and without noise) are already shown in Figs. 12 and 13. The results for other damage locations are presented in Fig. 14. As expected, the proposed method works well for different damage locations. Although spurious peaks arise with increasing noise, they are generally modest compared to the maximum peak due to the damage.

Next, the sensitivity of the proposed method to the severity of damage is investigated by reducing the elastic modulus E to 80%, 95%, and 98% of its original value. For brevity, only a 0.25 m damage at location D3 with data from sensor SM and a 5 m/s vehicle is analyzed herein. The 80% case is examined in Section 5.1 (see Figs. 12 and 13), while results for other damaged entities are reported in

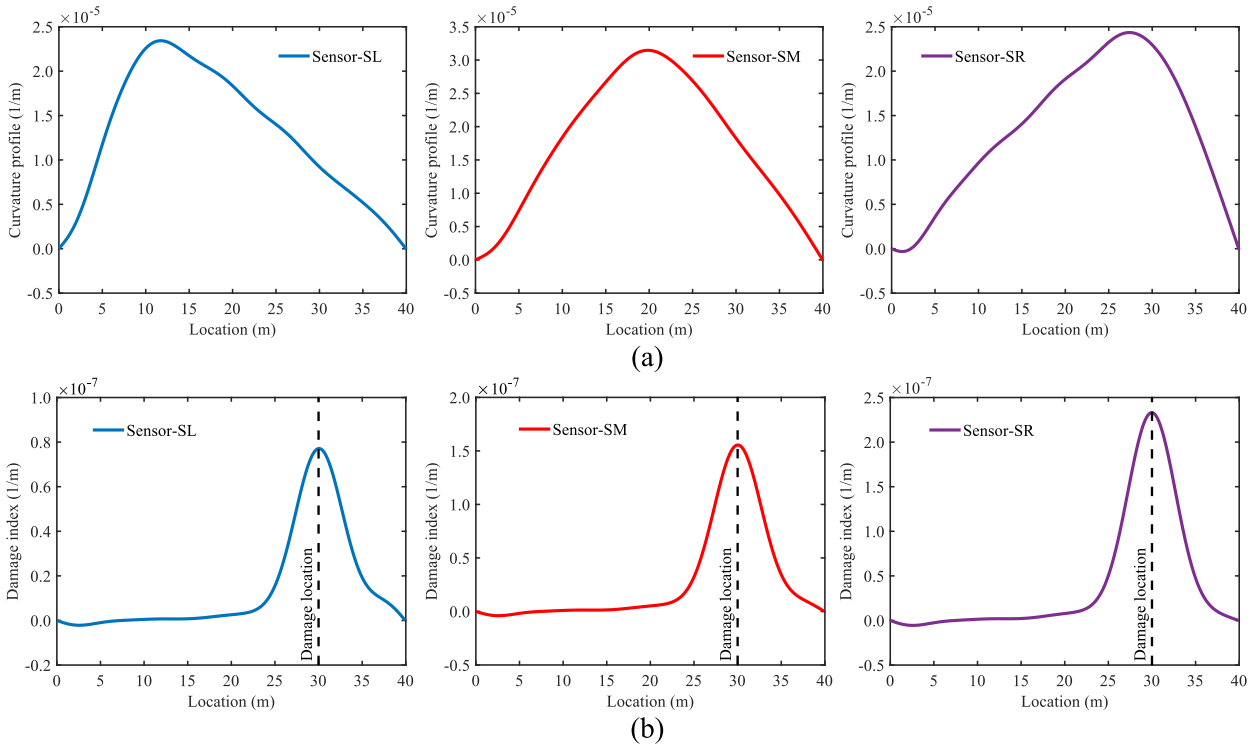

Fig. 12. Identification results for different sensor positions: (a) baseline curvature profile, (b) damage index.

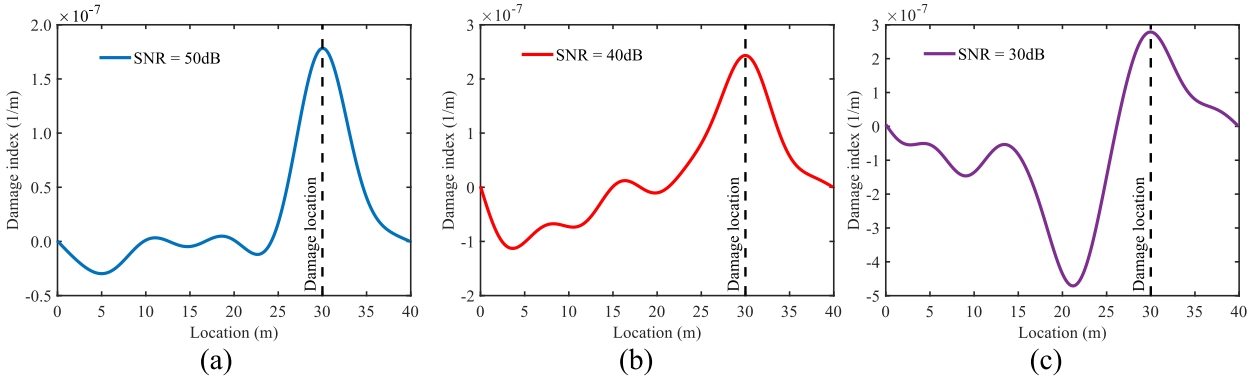

Fig. 13. Damage index obtained with noisy data: (a) SNR = 50 dB, (b) SNR = 40 dB, (c) SNR = 30 dB.

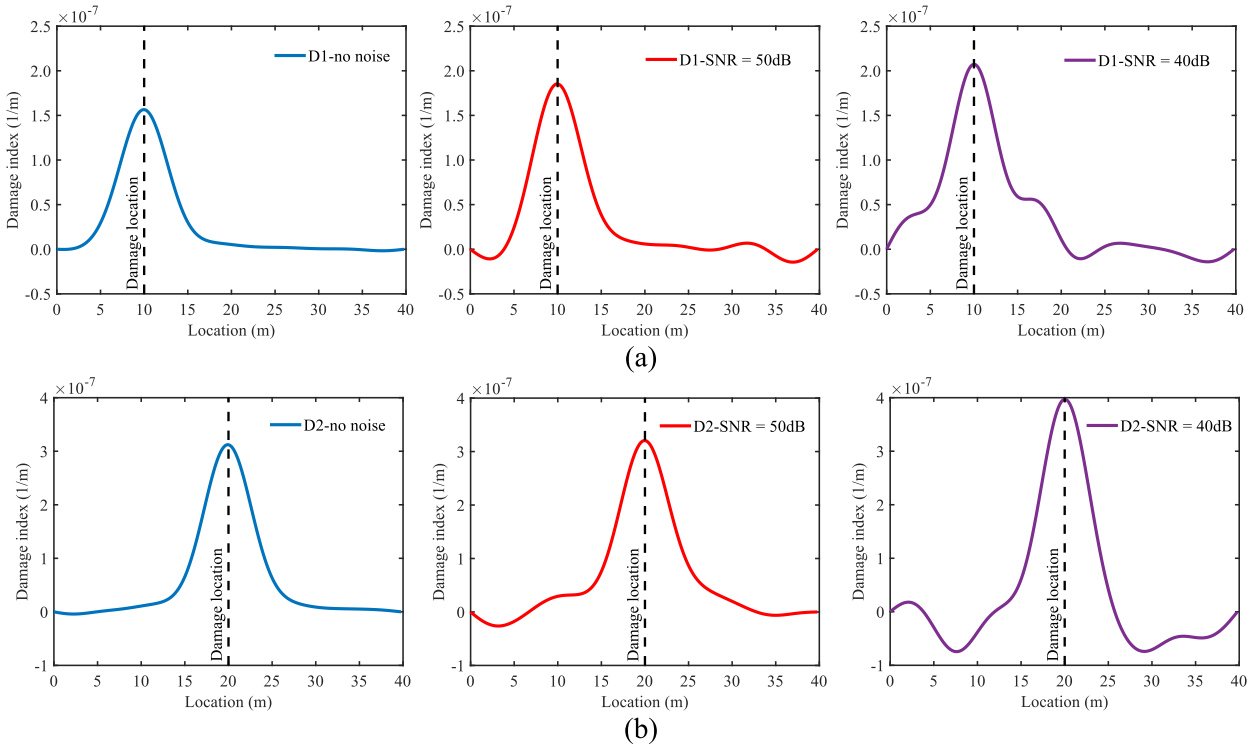

Fig. 14. Damage index obtained for different damage locations and noise levels: (a) D1, (b) D2.

Fig. 15. These results demonstrate that, in the analyzed scenario, the proposed method can theoretically detect very small degrees of damage, even 2%. Moreover, the magnitude of the damage index increases approximately proportionally with the damage severity. Although the localization capability decreases with lower SNR, the damage-induced peak remains distinguishable in most cases.

The impact of the damage extension on the proposed damage index is also investigated. Specifically, damage extensions of 0.25 m, 2 m, and 4 m, located around D3, are analyzed using data from the SM sensor with a 5 m/s vehicle. The first case (0.25 m) is discussed in Section 5.1 (see Figs. 12 and 13), while results for the other cases are presented in Fig. 16. The results show that the peak of the damage index consistently aligns with the center of the damaged region. As the damage length increases, the peak value of the damage index also rises, reflecting the sensitivity of the method to the overall damage severity. Notably, the influence of noise reduces as the damage extension increases.

Finally, a multiple-damage scenario is analyzed, involving two damaged regions of 0.25 m located at positions D1 and D3 (see Fig. 4). Each damage is modeled as a 20% reduction of E. Acceleration signals are collected from sensor SM, and the vehicle speed is set to 5m/s. Fig. 17 presents the results for the double-damage condition under different noise levels. In all three cases, the two damage locations can be identified accurately. Furthermore, fluctuations are induced by noise similar to the previous analyses.

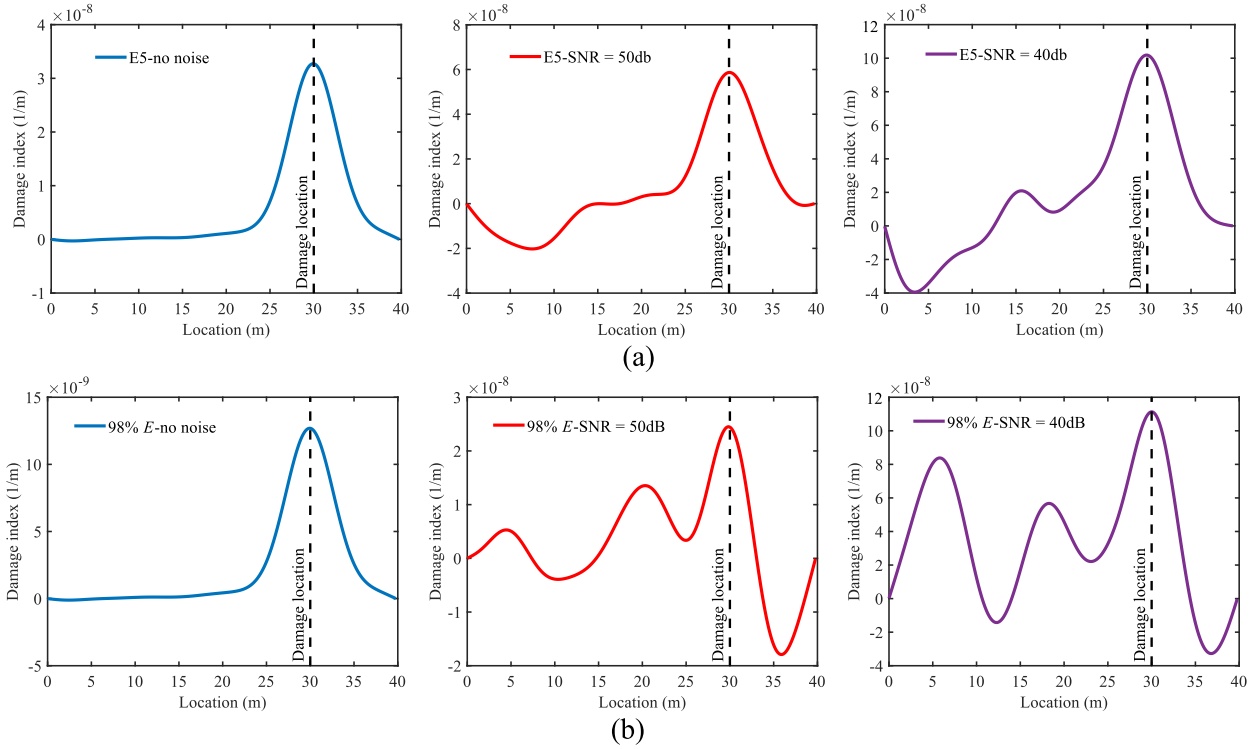

Fig. 15. Damage index obtained for different damage entities and noise levels: (a) *E* reduced to 95%, (b) *E* reduced to 98%.

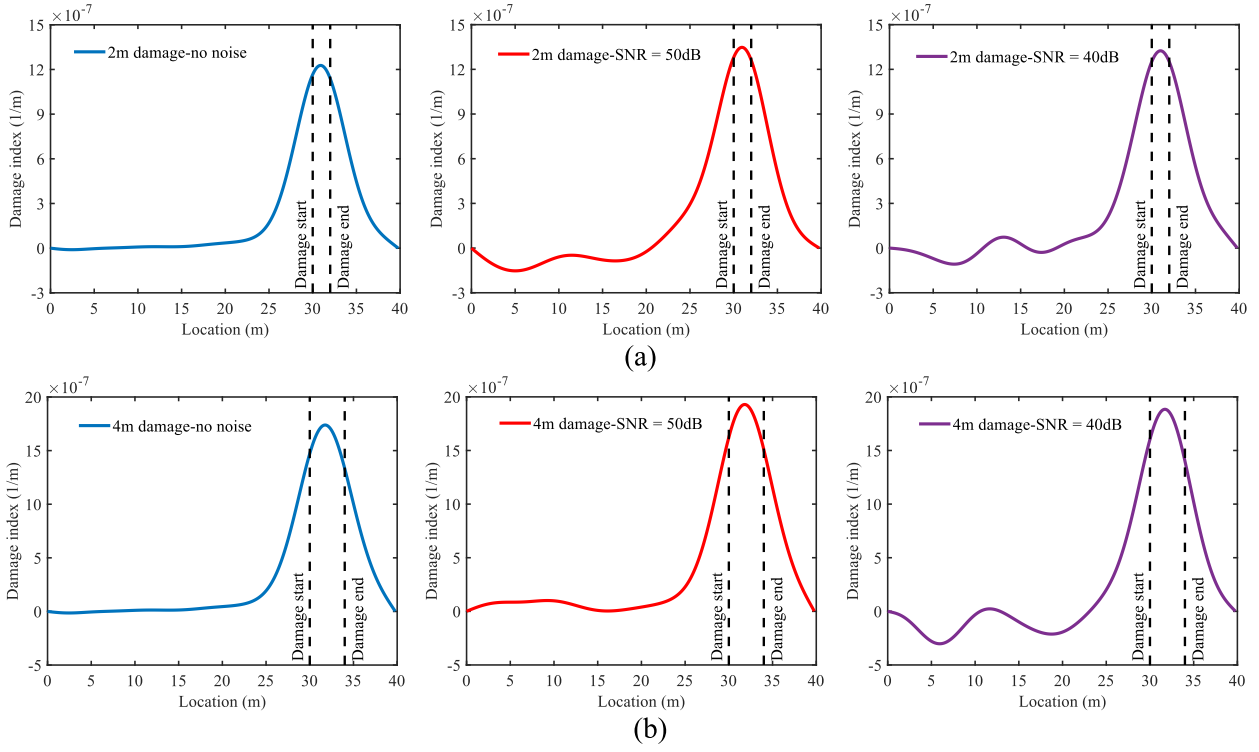

Fig. 16. Damage index obtained for different damage lengths and noise levels: (a) 2m, (b) 4m.

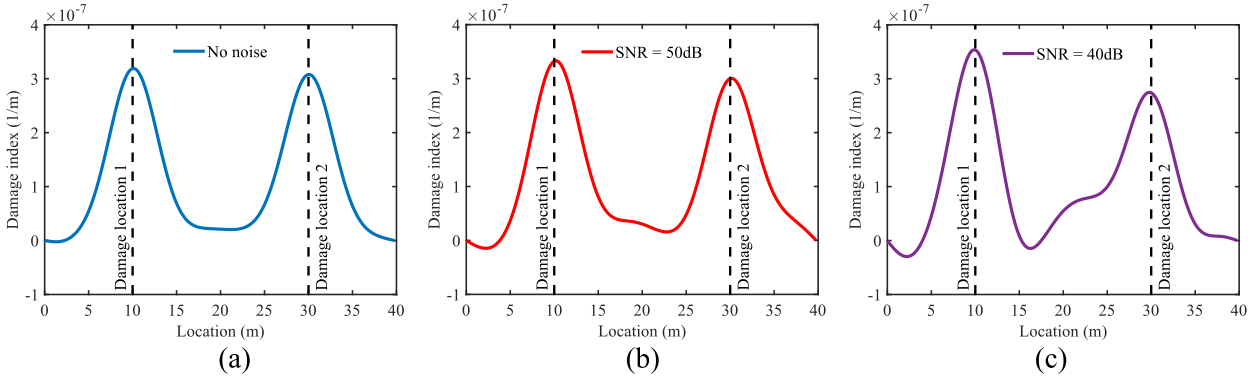

Fig. 17. Damage index obtained for the double-damage condition: (a) no noise, (b) SNR = 50 dB, (c) SNR = 40 dB.

5.3. Sensitivity to vehicle speed

Vehicle speed is a critical parameter in the proposed method, as the conventional approach based on low-pass filtering demonstrated high sensitivity to it, limiting its applicability to relatively modest speeds. In this section, two cases are analyzed with vehicle speeds equal to 40 km/h and 80 km/h, the results of which are shown in Fig. 18. The maximum frequency thresholds of the proposed method are selected as 0.8 and 1.05 for 40 km/h and 80 km/h, respectively.

As expected, increasing the vehicle speed significantly amplifies spurious peaks caused by dynamic components of the structural response. However, localization accuracy remains unaffected. These findings underscore the superior ability of the CWT to effectively separate dynamic and quasi-static components.

6. Real benchmark

To assess the generality of the proposed damage localization method, acceleration data from field monitoring of a real bridge, the

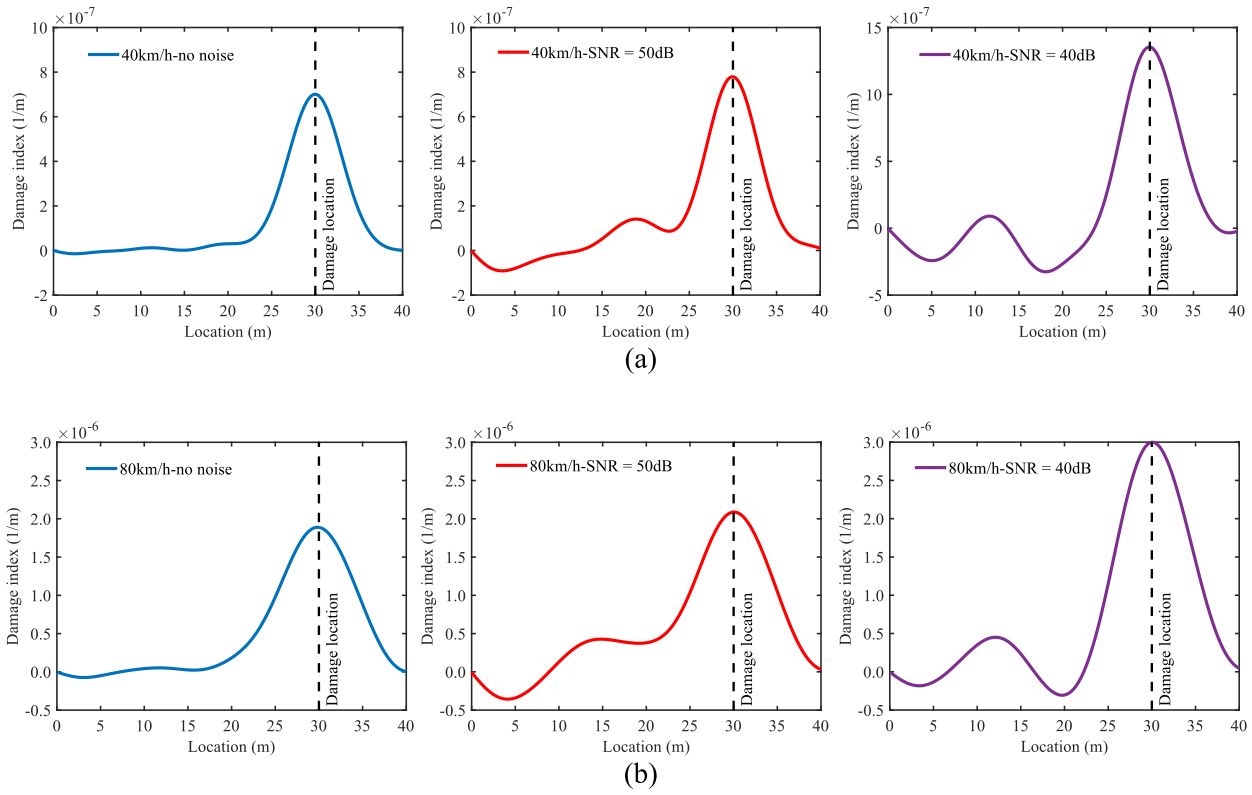

Fig. 18. Damage index obtained for typical operational speeds and noise levels: (a) 40 km/h, (b) 80km/h.

Old ADA Bridge in Japan [46], are used in this section. The analyzed bridge is illustrated in Fig. 19.

The structure is a simply-supported steel truss bridge with a main span of 59.2 m. The speed of the vehicle in the tests is approximately a constant of 40 km/h, and its axle spacing is 2.7 m. Four scenarios are considered in this field test, each obtained by artificially inducing a different damage configuration to the structure:

- Case A, Intact: no damage condition;
- Case B, Damage 1: 50% cross-sectional reduction of the element at midspan on one side of the deck (T1, see Fig. 19);
- Case C, Damage 2: 100% cross-sectional reduction of the same element considered in Case B;
- Case D, Recovery, repair of the cut vertical member through soldering;
- Case E, Damage 3, 100% cross-sectional reduction of the vertical element at 5/8 of the span on one side of the deck (T2, see Fig. 19).

For each case, 10 vertical acceleration time histories are collected by 5 sensors on the side of the damaged truss member (A1 to A5, see Fig. 19(b)) with a sampling frequency of 200 Hz. More details can be found in Ref. [46].

It is worth noting that the structure considered in this case study is not a strictly simply supported beam with a uniform cross-section. As a result, the expected quasi-static component of the bridge acceleration cannot be strictly interpreted as a curvature profile induced by a point load and may not be triangular. Reference curvature shapes for such configurations can be found in previous studies [22].

Fig. 20(a) and (b) show the mean quasi-static profiles obtained from different sensors for cases A and B. Although the profiles deviate from ideal triangular shapes (due to the specific geometry of the truss structure), the peak values consistently occur at the sensor locations, in agreement with the numerical results presented in Section 5.1.

Fig. 20(c) to (e) display the damage index values obtained using different sensor configurations. Specifically, panel (c) presents the damage index at the central sensor, while panels (d) and (e) show the sum of damage indexes from all five analyzed positions and from only the two lateral sensors, respectively.

It is important to note that, due to the structural characteristics of the steel truss bridge, the resulting damage index patterns differ from those observed in the numerical benchmark of beam-like bridges. In this case, the imposed damage (achieved by reducing the depth of a truss member) produces index profiles that do not exhibit the typical single-peak shape commonly seen in beam structures. Instead, the truss bridge shows a more complex distribution, reflecting load-path redistribution within the structural system. While using a single sensor (Fig. 20(c)) may lead to a slightly distorted estimate of the maximum variation of the quasi-static feature, combining information from multiple sensors provides a clearer and more accurate identification of the damage location.

Similarly, Fig. 21 presents the results obtained between scenarios A and C, which also show a positive correlation between the severity of damage and the corresponding damage index. This behavior also aligns with the results reported in Section 5.2.

Fig. 22 presents the damage index results comparing scenarios D and E. In this case, the damage index peak shifts toward the location of the damaged element, demonstrating responsiveness to different damage locations. However, accurate detection requires data from multiple sensors, even if they are not positioned directly at the damaged location, as illustrated in panel (c).

7. Conclusions

A novel damage localization method for bridges is proposed in this study, leveraging curvature profiles derived from structural acceleration responses via the continuous wavelet transform. Compared to state-of-the-art low-pass filtering approaches, the proposed method offers a flexible threshold strategy and enables more accurate and stable curvature profile extraction, particularly under high-speed conditions. This improvement contributes to more efficient and sustainable infrastructure monitoring and management.

A comprehensive parametric study, considering sensor position, noise level, and vehicle speed, confirms the robustness of the approach for simply supported bridges. Field validation further demonstrates its applicability to actual non-ideal beam bridge structures.

It is worth noting that several assumptions are made in this study. First, the simplified single-axle vehicle model may not fully represent real traffic conditions. Second, the method is applied only to statically determinate structures. These limitations will be

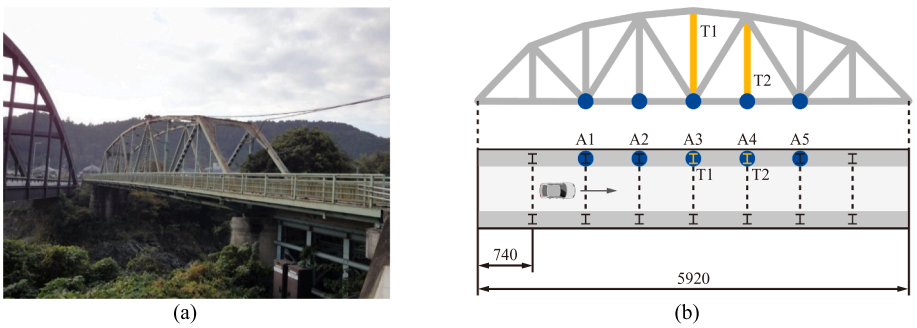

Fig. 19. Real bridge benchmark: (a) picture of the old ADA bridge (from [27]), (b) scheme of the tested bridge and sensor setup (dimensions in cm).

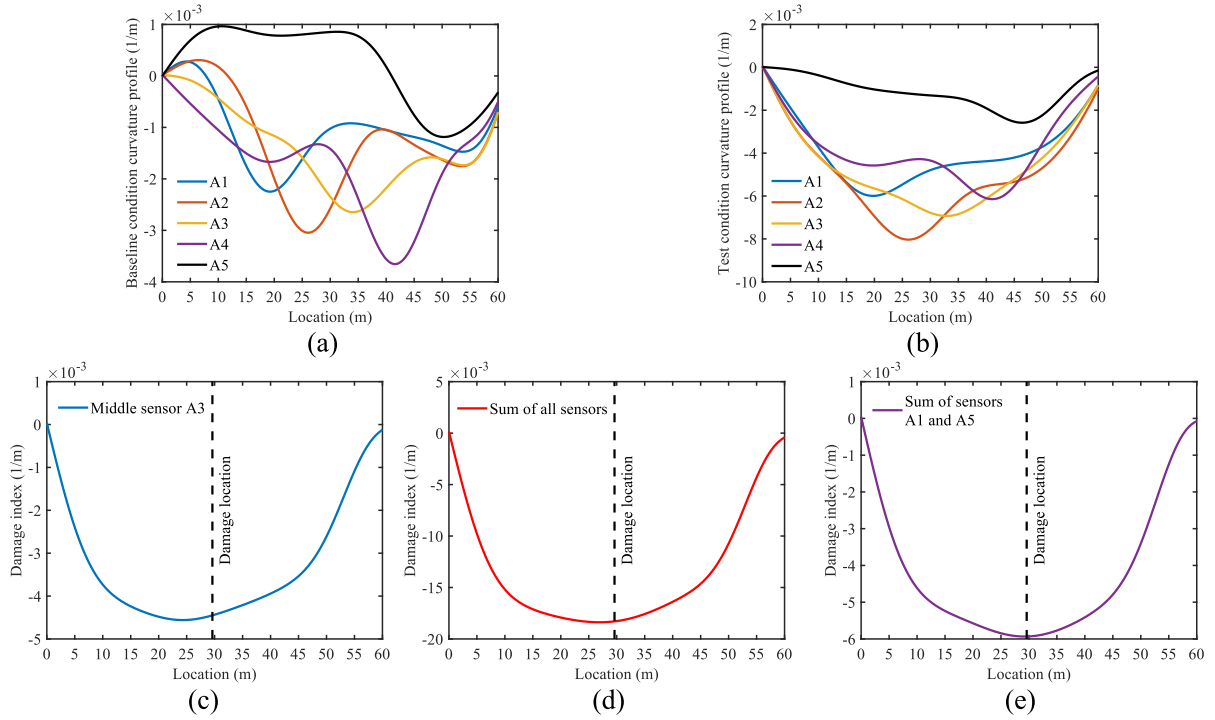

Fig. 20. Results for Cases A and B: (a) curvature profiles identified in the baseline condition (Case A), (b) curvature profiles identified in the test condition (Case B), (c) damage index obtained considering only sensor A3, (d) damage index obtained considering all sensors, (e) damage index obtained considering sensors A1 and A5.

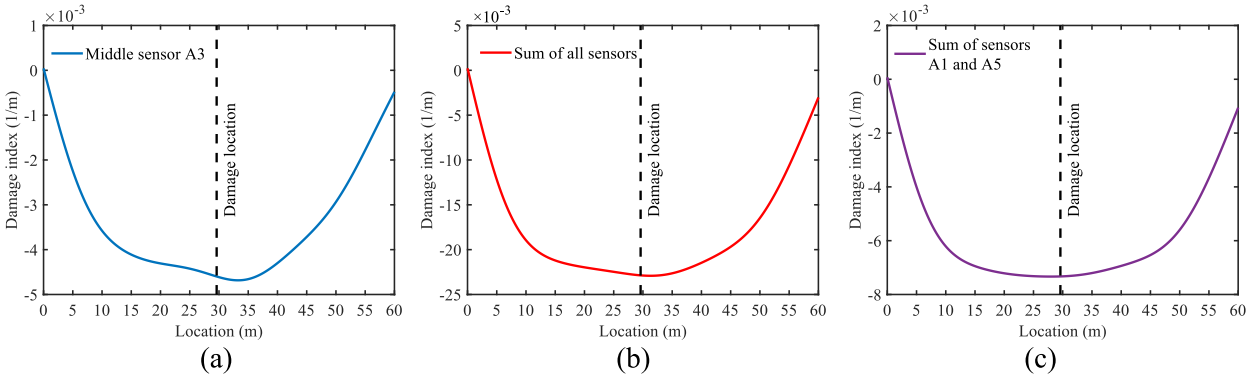

Fig. 21. Damage indices obtained for case C: (a) considering only sensor A3, (b) considering all sensors, (c) considering sensors A1 and A5.

further investigated in future studies.

CRediT authorship contribution statement

Sheng-Wang Zhang: Writing – original draft, Software, Methodology, Conceptualization. **Said Quqa:** Writing – review & editing, Supervision, Methodology, Conceptualization. **Antonio Palermo:** Writing – review & editing, Formal analysis. **Alessandro Marzani:** Writing – review & editing, Supervision. **Zhao-Hui Lu:** Writing – review & editing, Supervision, Funding acquisition.

Declaration of competing interest

The authors declare the following financial interests/personal relationships which may be considered as potential competing interests: Sheng-Wang Zhang reports financial support was provided by China Scholarship Council. Said Quqa and Alessandro Marzani report financial support was provided by European Union. Zhao-Hui Lu reports financial support was provided by the National Key

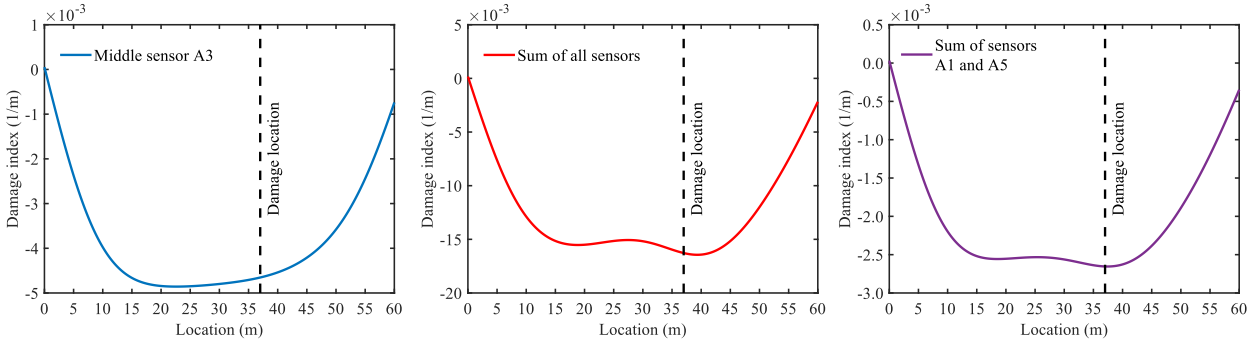

Fig. 22. Damage indices obtained for case E: (a) considering only sensor A3, (b) considering all sensors, (c) considering sensors A1 and A5.

R&D Program of China and the 111 Project. If there are other authors, they declare that they have no known competing financial interests or personal relationships that could have appeared to influence the work reported in this paper.

Acknowledgments

The study is partially supported by the National Key R&D Program of China (Grant Nos.: 2023YFC3805100 and 2023YFC3805101), the China Scholarship Council (Grant No.: 202306540057), and the 111 Project (Grant No.: D21001).

Part of the study was carried out within the MOST – Sustainable Mobility National Research Center and received funding from the European Union Next Generation EU (PIANO NAZIONALE DI RIPRESA E RESILIENZA (PNRR) – MISSIONE 4 COMPONENTE 2, INVESTIMENTO 1.4 – D.D. 1033 del 17/06/2022, CN00000023).

Appendix A. Vehicle-bridge interaction model

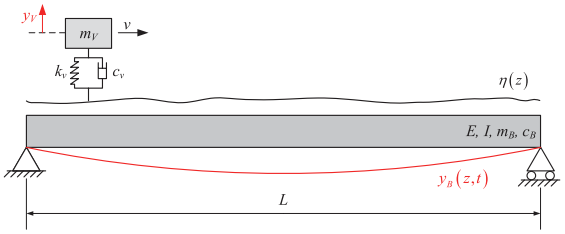

Fig. A.1. Scheme of the VBI system.

A VBI system [47] is considered in this study, which includes a bridge subjected to a vehicle moving with a constant speed v along the axis of the bridge, as shown in Fig. A.1. In this model, the vehicle is simplified as a sprung-mass system with mass m_V, spring stiffness k_V, and viscous damping c_V. The road profile of the bridge is modeled as a line with irregularity $\eta(z)$. The bridge is regarded as a simply supported beam with a length of L. The equations of the VBI system can be described as [48]:

$$EI\frac{\partial^4 y_B(z,t)}{\partial z^4}+m_B\frac{\partial^2 y_B(z,t)}{\partial t^2}+c_B\frac{\partial y_B(z,t)}{\partial t}=\delta(z-vt)f(t) \tag{A.1}$$

$$m_V\ddot{y}_V+c_V\left(\dot{y}_V-\dot{y}_B(z,t)-\dot{\eta}(z)\right)+k_V\left(y_V-y_B(z,t)-\eta(z)\right)=0 \tag{A.2}$$

where δ represents the Dirac delta function, EI is the flexural stiffness of the beam, given by the elastic modulus E and the moment of the cross-sectional inertia I, c_B denotes the damping coefficient of the bridge, and m_B is mass per unit length. In these equations, $y_B(z,t)$ is the structural vertical displacement, modeled as a function of space z and time t, y_v is the vertical position of the vehicle mass, while $f(t)$ is the force impressed by the vehicle on the beam, which can be expressed as:

$$f(t)=-m_V\left(g+\ddot{y}_V\right) \tag{A.3}$$

where g is the acceleration of gravity. The dot notation indicates derivation in time.

According to the superposition principle, the vertical displacement of the bridge excited by the moving vehicle can be written as a linear combination of modal responses:

$$y_B(z,t) = \sum_{m=1}^{\infty} \phi_m(z) q_m(t) \tag{A.4}$$

where $\phi_m(x)$ is the m-th mode shape, and $q_m(t)$ is the m-th displacement time history in the modal coordinates. For simply supported beams, the normalized mode shape can be written as:

$$\phi_m(z) = \sqrt{\frac{2}{L}} \sin\left(\frac{m\pi z}{L}\right) \tag{A.5}$$

Substituting Eqs. (A.4) and (A.5) into Eqs. (A.1) and (A.2), multiplying the equation by a mode ϕ_j, and integrating over z from 0 to L, the VBI system can be expressed as:

$$\begin{aligned} & m_B \ddot{q}_m + 2 m_B \xi_m \omega_{B,m} \dot{q}_m + m_B \omega_{B,m}^2 q_m \\ & = c_V \phi_j \left(\dot{y}_V - \dot{\eta} - \sum_{m=1}^{\infty} \phi_m \dot{q}_m - \sum_{m=1}^{\infty} v \phi_m' q_m \right) + k_V \phi_j \left(y_V - \eta - \sum_{m=1}^{\infty} \phi_m q_m \right) - m_V g \phi_j \end{aligned} \tag{A.6}$$

$$m_V \ddot{y}_V + c_V \dot{y}_V + k_V y_V - c_V \sum_{m=1}^{\infty} \phi_m \dot{q}_m - c_V \sum_{m=1}^{\infty} v \phi_m' q_m - k_V \sum_{m=1}^{\infty} \phi_m q_m = c_V \dot{\eta} + k_V \eta \tag{A.7}$$

where the prime notation indicates derivation in space, $\omega_{B,m}$ is the m-th natural frequency of the bridge, and ξ_m is the corresponding damping ratio, which can be expressed as follows:

$$\omega_{B,m} = \left(\frac{m\pi}{L}\right)^2 \sqrt{\frac{EI}{m_B}} \tag{A.8}$$

$$\xi_m = \frac{c_B}{2 m_B \omega_{B,m}} \tag{A.9}$$

The acceleration response of the bridge can be solved numerically, for instance, using the Newmark-beta method.

Data availability

Data will be made available on request.

References

[1] M.Z. Sarwar, D. Cantero, Deep autoencoder architecture for bridge damage assessment using responses from several vehicles, Eng. Struct. 246 (2021) 113064.
[2] S.S. Saidin, A. Jamadin, S. Abdul Kudus, N. Mohd Amin, M.A. Anuar, An overview: the application of vibration-based techniques in bridge structural health monitoring, Int. J. Concr. Struct. M. 16 (1) (2022) 69.
[3] O. Avci, O. Abdeljaber, S. Kiranyaz, M. Hussein, M. Gabbouj, D.J. Inman, A review of vibration-based damage detection in civil structures: from traditional methods to machine learning and deep learning applications, Mech. Syst. Signal Process. 147 (2021) 107077.
[4] A.S. Nobari, M.F. Aliabadi, Vibration-based Techniques for Damage Detection and Localization in Engineering Structures, World Scientific, 2018.
[5] V. Alves, A. Cury, An automated vibration-based structural damage localization strategy using filter-type feature selection, Mech. Syst. Signal Process. 190 (2023) 110145.
[6] A.A. Mousavi, C.W. Zhang, S.F. Masri, G. Gholipour, Damage detection and localization of a steel truss bridge model subjected to impact and white noise excitations using empirical wavelet transform neural network approach, Measurement 185 (2021) 110060.
[7] S. Quqa, L. Landi, Damage localization in a steel truss bridge using influence lines identified from vehicle-induced acceleration, J. Bridge. Eng. 28 (4) (2023) 04023012.
[8] X. Zheng, D.H. Yang, T.H. Yi, H.N. Li, Development of bridge influence line identification methods based on direct measurement data: a comprehensive review and comparison, Eng. Struct. 198 (2019) 109539.
[9] C.R. Farrar, K. Worden, Structural Health Monitoring: A Machine Learning Perspective, John Wiley & Sons, 2012.
[10] Z.W. Chen, L. Zhao, J. Zhang, Q.L. Cai, J. Li, S. Zhu, Damage quantification of beam structures using deflection influence line changes and sparse regularization, Adv. Struct. Eng. 24 (9) (2021) 1997–2010.
[11] X. Zheng, D.H. Yang, T.H. Yi, H.N. Li, Bridge influence line identification from structural dynamic responses induced by a high-speed vehicle, Struct. Control. Health. Monit. 27 (7) (2020) e2544.
[12] Z.W. Chen, Z.C. Guo, W.X. Ren, Y. Zhang, A novel bridge influence line identification approach based on nonlinear frequency modulation signal reconstruction, Mech. Syst. Signal Process. 219 (2024) 111622.
[13] J.S. Zhu, C. Zhang, X.T. Li, Structural damage detection of the bridge under moving loads with the quasi-static displacement influence line from one sensor, Measurement. 211 (2023) 112599.
[14] N.B. Wang, C. Wang, H. Zhou, Q. Zuo, A novel extraction method for the actual influence line of bridge structures, J. Sound. Vib. 553 (2023) 117605.
[15] L.M. Sun, W. Zhang, S. Nagarajaiah, Bridge real-time damage identification method using inclination and strain measurements in the presence of temperature variation, J. Bridge. Eng. 24 (2) (2019) 04018111.
[16] Z.W. Chen, S.Y. Zhu, Y.L. Xu, Q. Li, Q.L. Cai, Damage detection in long suspension bridges using stress influence lines, J. Bridge. Eng. 20 (3) (2015) 05014013.
[17] B.T. Wu, G. Wu, C.Q. Yang, Y. He, Damage identification method for continuous girder bridges based on spatially-distributed long-gauge strain sensing under moving loads, Mech. Syst. Signal Process. 104 (2018) 415–435.
[18] H.H. Nassif, M. Gindy, J. Davis, Comparison of laser Doppler vibrometer with contact sensors for monitoring bridge deflection and vibration, Ndt&E Int 38 (3) (2005) 213–218.

[19] M.M. Alamdari, K. Kildashti, B. Samali, H.V. Goudarzi, Damage diagnosis in bridge structures using rotation influence line: validation on a cable-stayed bridge, Eng. Struct. 185 (2019) 1–14.
[20] E.J. Obrien, J. Brownjohn, D. Hester, F. Huseynov, M. Casero, Identifying damage on a bridge using rotation-based bridge weigh-in-motion, J. Civil Struct. Health Monit. 11 (1) (2021) 175–188.
[21] S. Quqa, A. Antolini, E.F. Scarselli, A. Gnudi, A. Lico, M. Carissimi, M. Pasotti, R. Canegallo, L. Landi, P.P. Diotallevi, Phase change memories in smart sensing solutions for structural health monitoring, J. Comput. Civ. Eng. 36 (4) (2022) 04022013.
[22] S. Quqa, M.A. Siddiqui, F. Zonzini, A. Palermo, Identification of bridge curvature profiles from dynamic responses induced by moving vehicles using autoregressive models, Mech. Syst. Sign. Proc. 241 (2025) 113553.
[23] S. Quqa, L. Landi, P.P. Diotallevi, Automatic identification of dense damage-sensitive features in civil infrastructure using sparse sensor networks, Autom. Constr. 128 (2021) 103740.
[24] X.Z. Lu, L.M. Sun, K.C. Chang, C.W. Kim, Z.R. Han, Damage localization using low-frequency bridge acceleration component under a moving vehicle, Eng. Struct. 325 (2025) 119366.
[25] C.M. Akujuobi, Wavelets and wavelet transform systems and their applications, Springer, 2022.
[26] X.Q. Zhu, S.S. Law, Wavelet-based crack identification of bridge beam from operational deflection time history, Int. J. Solids Struct. 43 (7–8) (2006) 2299–2317.
[27] Z.H. Nie, H. Zhang, Z.M. Zhu, H.W. Ma, Baseline-free bridge damage identification using proper orthogonal decomposition and continuous wavelet transform with limited sensors, J. Sound. Vib. 605 (2025) 119012.
[28] J.L. Liu, S.F. Wang, Y.Z. Li, A.H. Yu, Time-varying damage detection in beam structures using variational mode decomposition and continuous wavelet transform, Constr. Build. Mater. 411 (2024) 134416.
[29] J.S. Zhu, S. Zhou, Influence line identification method based on VMD combined with improved wavelet threshold denoising, Int. J. Struct. Stab. Dyn. 24 (19) (2024) 2450215.
[30] D. Hester, A. González, A wavelet-based damage detection algorithm based on bridge acceleration response to a vehicle, Mech. Syst. Signal Process. 28 (2012) 145–166.
[31] V. Shahsavari, L. Chouinard, J. Bastien, Wavelet-based analysis of mode shapes for statistical detection and localization of damage in beams using likelihood ratio test, Eng. Struct. 132 (2017) 494–507.
[32] L. Debnath, F.A. Shah, Wavelet transforms and their applications, Springer, 2015.
[33] M.A. Pinsky, Introduction to Fourier analysis and wavelets, Am. Math. Soc. (2023).
[34] L. Frýba, Vibration of solids and structures under moving loads, Thomas Telford London, 1999.
[35] M. Vetterli, J. Kovacevic, Wavelets and subband coding, Prentice Hall PTR Englewood Cliffs, NJ, 1995.
[36] J.M. Lilly, S.C. Olhede, Generalized Morse wavelets as a superfamily of analytic wavelets, IEEE Trans. Signal. Process. 60 (11) (2012) 6036–6041.
[37] J.M. Lilly, S.C. Olhede, Higher-order properties of analytic wavelets, IEEE Trans. Signal. Process. 57 (1) (2008) 146–160.
[38] E.A. Martinez-Ríos, R. Bustamante-Bello, S.A. Navarro-Tuch, Generalized Morse wavelets parameter selection and transfer learning for pavement transverse cracking detection, Eng. Appl. Artif. Intell. 123 (2023) 106355.
[39] J.M. Lilly, Element analysis: A wavelet-based method for analysing time-localized events in noisy time series, Proc. Royal Soc. A: Math., Phys. Eng. Sci. 473 (2200) (2017) 20160776.
[40] G. Strang, T. Nguyen, Wavelets and filter banks, Wellesley-Cambridge Press, Wellesley, 1996.
[41] J. Gomes, L. Velho, From Fourier analysis to wavelets, Springer, 2015.
[42] J.Y. Ren, Y.H. Chen, Z.Q. Sun, Y. Zhang, A vehicle-bridge interaction vibration model considering bridge deck pavement, J. Low Frequency Noise, Vibration Active Control 42 (1) (2023) 146–172.
[43] I. Standard, Mechanical vibration-road surface profiles-reporting of measured data, ISO Standard (2016).
[44] P. Múčka, Simulated road profiles according to ISO 8608 in vibration analysis, J. Test. Eval. 46 (1) (2018) 405–418.
[45] K.K. Paliwal, A noise-compensated long correlation matching method for AR spectral estimation of noisy signals, Signal Processing 15 (4) (1988) 437–440.
[46] C.W. Kim, F.L. Zhang, K.C. Chang, P.J. McGetrick, Y. Goi, Ambient and vehicle-induced vibration data of a steel truss bridge subject to artificial damage, J. Bridge. Eng. 26 (7) (2021) 04721002.
[47] D. Cantero, VBI-2D–road vehicle-bridge interaction simulation tool and verification framework for Matlab, SoftwareX. 26 (2024) 101725.
[48] Y.B. Yang, M.C. Cheng, K.C. Chang, Frequency variation in vehicle-bridge interaction systems, Int. J. Struct. Stab. Dyn. 13 (02) (2013) 1350019.